

PAPER • OPEN ACCESS

The pseudoatomic orbital basis: electronic accuracy and soft-mode distortions in ABO_3 perovskites

To cite this article: Jack S Baker *et al* 2020 *Electron. Struct.* **2** 025002

View the [article online](#) for updates and enhancements.

Electronic Structure

OPEN ACCESS**PAPER**

The pseudoatomic orbital basis: electronic accuracy and soft-mode distortions in ABO_3 perovskites

RECEIVED
10 March 2020**REVISED**
7 May 2020**ACCEPTED FOR PUBLICATION**
20 May 2020**PUBLISHED**
24 June 2020

Original content from this work may be used under the terms of the [Creative Commons Attribution 4.0 licence](#).

Any further distribution of this work must maintain attribution to the author(s) and the title of the work, journal citation and DOI.

Jack S Baker^{1,2,4} , Tsuyoshi Miyazaki³ and David R Bowler^{1,2,3} ¹ London Centre for Nanotechnology, UCL, 17-19 Gordon St, London WC1H 0AH, United Kingdom² Department of Physics & Astronomy, UCL, Gower St, London WC1E 6BT, United Kingdom³ International Centre for Materials Nanoarchitectonics (MANA), National Institute for Materials Science (NIMS), 1-1 Namiki, Tsukuba, Ibaraki 305-0044, Japan⁴ Author to whom any correspondence should be addressed.**E-mail:** jack.baker.16@ucl.ac.uk, MIYAZAKI.Tsuyoshi@nims.go.jp and david.bowler@ucl.ac.uk**Keywords:** perovskite, pseudoatomic orbitals, Bader, charge density, linear scaling, density functional theory, soft modesSupplementary material for this article is available [online](#)

Abstract

The perovskite oxides are known to be susceptible to structural distortions over a long wavelength when compared to their parent cubic structures. From an *ab initio* simulation perspective, this requires accurate calculations including many thousands of atoms; a task well beyond the remit of traditional plane wave-based density functional theory (DFT). We suggest that this void can be filled using the methodology implemented in the large-scale DFT code, CONQUEST, using a local pseudoatomic orbital (PAO) basis. Whilst this basis has been tested before for some structural and energetic properties, none have treated the most fundamental quantity to the theory, the charge density $n(\mathbf{r})$ itself. An accurate description of $n(\mathbf{r})$ is vital to the perovskite oxides due to the crucial role played by short-range restoring forces (characterised by bond covalency) and long range Coulomb forces as suggested by the soft-mode theory of Cochran and Anderson. We find that modestly sized basis sets of PAOs can reproduce the plane-wave charge density to a total integrated error of better than 0.5% and provide Bader partitioned ionic charges, volumes and average charge densities to similar degree of accuracy. Further, the multi-mode antiferroelectric distortion of $PbZrO_3$ and its associated energetics are reproduced by better than 99% when compared to plane-waves. This work suggests that electronic structure calculations using efficient and compact basis sets of pseudoatomic orbitals can achieve the same accuracy as high cutoff energy plane-wave calculations. When paired with the CONQUEST code, calculations with high electronic and structural accuracy can now be performed on many thousands of atoms, even on systems as delicate as the perovskite oxides.

1. Introduction

The ABO_3 perovskite oxides are well known for their vast and rich variety of physical phenomena. These include interfacial two-dimensional electron gases [1, 2], negative capacitance [3, 4], high-temperature superconductivity [5, 6] and many more. Many of these are linked to a plethora of responsible order parameters and their competition/coupling with one another [7, 8]. Ferroelectric, ferromagnetic antiferroelectric & antiferromagnetic order are all commonplace in the perovskite oxides as well as antiferrodistortions (rotations of the BO_6 octahedra) and Jahn–Teller distortions. Some of these features are also known to coexist with one another giving rise to the phenomena of multiferrocity [9]. In simulation, the onset of many different competing order parameters can create a myriad of distinct local minima with similar energetics. It is then of paramount importance that our simulation methodology produces accurate results such that we can distinguish them from one another in their energetics but also accurately resolve their electronic & structural properties.

In addition to the requirement of high accuracy, the perovskite oxides present structural and magnetic features over a long wavelength requiring first principles simulations of thousands of atoms. For example, thin ferroelectric films are known to form *flux-closure domains* as a compensation mechanism for the depolarising field [10, 11]. The domain period in these films increases also with the depth of the film in question (the well known Kittel scaling law) thus requiring simulations in excess of a thousand atoms. In the case of multiferroic BiFeO₃, the competition between various exchange interactions manifests in the softening of a 64 nm non-collinear spin-cycloid [12, 13] and a unit cell of ~ 1000 atoms. Current simulations often bypass this fact and approximate this complex magnetic order as simple G-type antiferromagnetism. Studies of solid-solution families (AB_xC_{1-x}O₃, (1-x)ABO₃ - xCDO₃ and more) are popular in the field. Large supercell calculations can offer realistic experimental order of these alloys which can improve upon the accuracy of structural distortions found in smaller supercells and approximations like the virtual crystal approximation [14–16]. Further, longer wavelength dynamical instabilities are found to be competitive in the important piezoelectric solid solution PbZr_{0.5}Ti_{0.5}O₃ (PZT 50/50) requiring a large number of atoms to simulate the energetics [14].

Electronic structure calculations based on density functional theory (DFT) employing the plane-wave pseudopotential method [17, 18] are known to achieve accurate results. This is in part due to the systematic, variational nature of the plane-wave basis where increasing the number of basis functions is *guaranteed* to increase the level to which your calculations are converged. This method is not without its drawbacks. A plane-wave by itself (the solution of the free electron) bears little to no resemblance to the Kohn–Sham orbitals of the systems they are intended to represent. This is especially true for the localised 3d electrons of the transition metals, responsible for magnetic and orbital order. It is for this reason that many thousands of plane-waves are required in the basis set expansion at a great computational cost. Further, plane-waves span the whole of the simulation cell which introduces wasteful calculations on the grid for systems including a vacuum region. These issues can be bypassed by replacing plane-waves with physically intuitive local basis sets of pseudoatomic orbitals (PAOs) [19–23]. These are atomic-like orbitals for which the radial part is solved in the pseudopotential of each ionic species [24, 25]. PAOs are now regularly used in the *Siesta* [20], *OpenMX* [26] & *CONQUEST* [27] codes, the last of which is employed in this work. The construction and generation of such a basis is described in section 2.2.

Our PAOs are designed with a cut-off in real space (where the basis function becomes zero) motivated by the desire to employ efficient sparse matrix algebra with high parallel efficiency [28]. Further, our formulation of DFT is based on the density matrix $\rho(\mathbf{r}, \mathbf{r}')$. Should we choose to truncate the range of this matrix (a requirement should we wish to use the linear scaling mode of operation), we are physically supported by the principle of near-sightedness; the assertion that the density matrix $\rho(\mathbf{r}, \mathbf{r}')$ decays to zero as $|\mathbf{r} - \mathbf{r}'| \rightarrow \infty$ [29]. Complete with a change in algorithm (the scope of which is beyond this work but discussed in references [27, 30]), this allows the well known $\mathcal{O}(N^3)$ scaling wall (where N is the number of atoms in the simulation) in standard DFT to be broken and replaced with a code which now scales as $\mathcal{O}(N)$. This method paves the way for full electronic structure calculations on systems of many thousands of atoms (or even millions [31]), well beyond what is possible with conventional plane-wave methods. The *CONQUEST* code has recently become publicly available with an MIT license [32].

The accuracy of the PAO basis has been reported in previous works [22, 23, 33–35] including calculations of the structural parameters (bulk moduli and lattice constants) for this set of pseudopotentials [33]. Notably, none have reported on the effects to the most fundamental quantity in DFT; the charge density $n(\mathbf{r})$ itself. An accurate account of $n(\mathbf{r})$ is of a high importance for the perovskite oxides. Not only because applications require it (like the simulation of 2DEGs [36]) but because of the possible ramifications for the soft-mode theory of ferroelectricity [37, 38]. That is, the ferroelectric transition is governed by a zone centre dynamical instability driven by the competition of short range covalent forces (preferring cubic symmetry) and long range Coulomb forces (favouring the ferroelectric state). The charge density $n(\mathbf{r})$ (and its derived quantities) is clearly a probe of bond covalency [39, 40] whilst electron–electron Coulomb terms feature explicit dependence on $n(\mathbf{r})$ in the calculation of the Hartree potential [41].

It is the purpose of this work to quantify the performance of PAOs versus the plane-wave pseudopotential method using calculations with the same pseudopotential. We compare the groundstate charge densities and the order parameters controlling ferroelectric & antiferroelectric order. We do so by considering crystals of PbTiO₃ (PTO), PbZrO₃ (PZO) and two supercell arrangements of the solid solution PbZr_xTi_{1-x}O₃, $x = 0.5$ (PZT 50/50). PTO is a prototypical ferroelectric known to undergo a paraelectric to ferroelectric phase transition from cubic Pm $\bar{3}$ m to tetragonal P4mm below 763 K [42]. This phase transition is known to come about from the softening of a zone centre lattice mode of irreducible representation (irrep) Γ_4^- [42]. In contrast, PZO undergoes a paraelectric to antiferroelectric phase transition from cubic Pm $\bar{3}$ m to orthorhombic Pbam below 505 K [43]. This transition is also thought to be caused by soft lattice modes [43–46] but in this case has a more complex multi-mode description comprised primarily of R_4^+ , Σ_2 & S_4 modes [44,

45]. A small part of the distortion is also due to the softening of R_5^+ , X_3^- & M_5^- lattice modes [44, 45]. We quantify the amplitudes of each individual lattice mode (and strain modes, detailed in the supplemental material (<https://stacks.iop.org/EST/02/025002/mmedia>)) in the phase transitions of both perovskites as well determining the associated energetics for each of the considered PAO basis sets. Since the energy differences associated with the perovskite oxides are generally small (a few meV/atom), this is a *strict* test for the accuracy of PAOs.

The remainder of this work is now organized as follows. Within section 2.1, we outline the general simulation method for both the plane-wave and PAO DFT calculations and describe the phases of PTO, PZO & PZT 50/50 considered in the study. In section 2.2 we describe the method for the generation of the PAO basis set and the details of the basis sets used in this work. Section 3.1 provides charge density difference analysis between PAO calculations and plane-waves as well presenting the Bader analysis of the ionic charges, volumes and average densities. In section 3.2 we compare the amplitudes of the soft-mode distortions responsible for the ferroelectric and antiferroelectric phase transitions in the PTO & PZO including the energetics associated with crucial displacive modes. We also closely examine the energetics over the phase transition paths by steadily increasing mode amplitudes until a maximal value, then, cumulatively add the remaining important modes. We conclude this work in section 4 with a broad overview of our findings. This includes a discussion of the impact this work has on the topic of local basis sets and the promise of accurate and large-scale electronic structure calculations on the perovskite oxides.

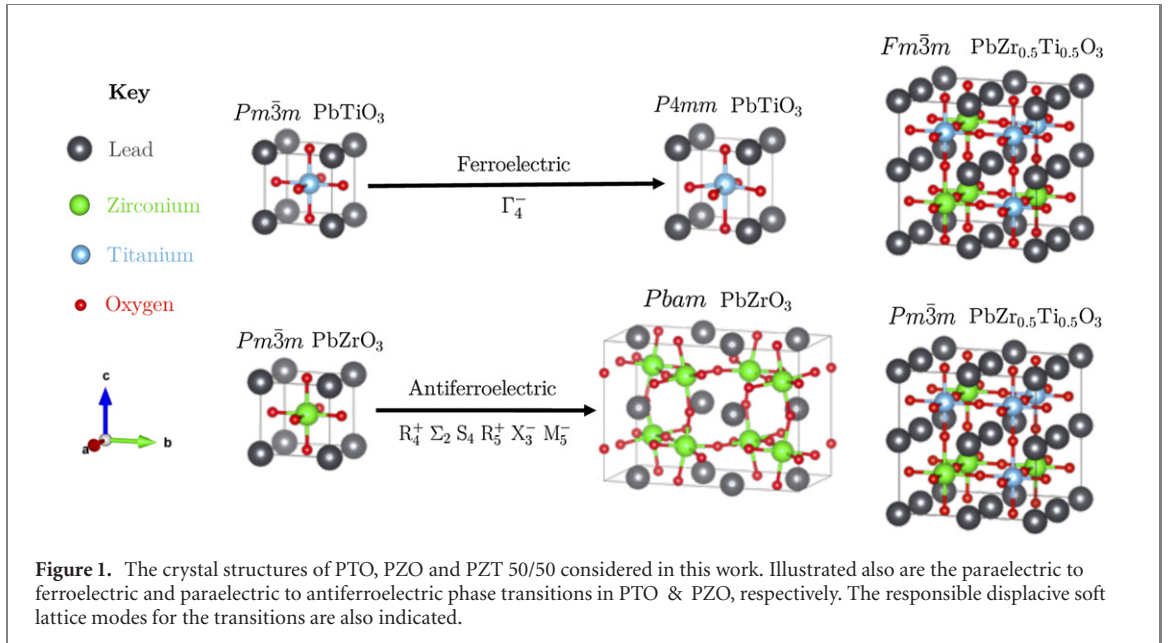
2. Theoretical method

2.1. Computational details

Calculations are performed using two different implementations of DFT. Calculations using the plane-wave basis set are performed with the ABINIT code [47, 48] (v8.10.2) whilst calculations utilising PAOs are carried out using the CONQUEST code (v1.0) [27, 32, 49] with the direct diagonalisation of the Hamiltonian matrix. Both codes are able to use the same norm-conserving pseudopotentials as produced by ONCVSP [50] (v3.3.1) where input parameters were taken from the library (v0.4) on the PseudoDojo website [51]. This library is known for its high accuracy results versus other pseudopotentials, projector augmented wave methods & all-electron results as characterised in the well known DFT *delta study* [18]. These pseudopotentials are scalar-relativistic and include partial core corrections. The Pb 5d, 6s, 6p, Ti 3s, 3p, 4s, 3d, Zr 4s, 4p, 5s, 5d and O 2s, 2p orbitals are treated as valence in the pseudopotentials, but, in the CONQUEST calculations the $n = 3/4$ states of Ti/Zr are treated as semi-core (see below). Exchange & correlation is represented by the PBEsol functional [52] as present in Libxc [53] (v3.0.0). This functional is known to produce accurate structural properties for many crystals including the perovskite oxides [54]. For the CONQUEST calculations, we consider three different basis sets with increasing accuracy. These are the single- ζ plus polarisation (SZP), double- ζ plus double-polarisation (DZDP) and triple- ζ plus triple-polarisation (TZTP) basis sets respectively. Semi-core states (like those present in Ti/Zr) include only a single- ζ per l -channel. This approach allows us to study the effect of systematically adding an extra ζ per angular momentum channel. The basis sets and details of their generation are described fully in section 2.2

The different crystal structures treated in this study are shown in figure 1. They display the cubic & tetragonal phases of PTO, the cubic & orthorhombic phases of PZO and two cubic arrangements of the PZT 50/50 solid solution. For cubic PZO, cubic PTO and tetragonal PTO, reciprocal space integrals are replaced with summations over a $9 \times 9 \times 9$ Monkhorst-pack [55] mesh whilst orthorhombic PZO and the cubic PZT 50/50 arrangements use a $7 \times 3 \times 5$ & $5 \times 5 \times 5$ mesh respectively. For structural relaxation, ABINIT calculations use a 40 Ha plane-wave cutoff and a 160 Ha cutoff on the charge density grid whilst CONQUEST calculations use a 300 Ha plane-wave-equivalent cutoff for both integrals on the grid and the charge density grid. These parameters were chosen that total energies are converged to better than 1 meV/ABO₃ formula unit. The ionic positions are relaxed until the magnitude of the maximum force on all ions falls below 5×10^{-3} eV Å⁻¹. Stresses are also relaxed until all elements of the Cartesian stress tensor fall below 1×10^{-4} GPa. This process is repeated for all considered crystals and for each basis set.

For calculations assessing the charge density (section 3.1), we use a finer charge density grid with $100 \times 100 \times 100$ grid points/ABO₃ formula unit. For the orthorhombic $\sqrt{2} \times 2\sqrt{2} \times 2$ PZO unit cell, we use $150 \times 300 \times 200$ grid points. Each of these finer charge density calculations, for each basis, are performed using the optimised plane-wave structure of each crystal. In order to assign ionic charges, volumes and average ionic densities, we use the Bader partitioning scheme as implemented in the Bader code [56–59] (v1.03). This code partitions individual atoms in crystals using the zero-flux surface of the charge density. This is a 2-D surface for which the charge density is at a minimum perpendicular to the surface. We note that whilst there is no unequivocal definition for the assignment of ionic charge, we choose the Bader definition



since it derives *only* from $n(\mathbf{r})$ thus introducing no new variables to our analysis. We define also a total integrated electronic error designed to quantify the level of disagreement in $n(\mathbf{r})$ for the plane-wave and PAO calculations. This is defined by the integral

$$N_{\text{error}}^e = \int |n_{\text{PAO}}(\mathbf{r}) - n_{\text{PW}}(\mathbf{r})| d\mathbf{r} \quad (1)$$

for plane-wave/PAO electronic charge density $n_{\text{PW}}(\mathbf{r})/n_{\text{PAO}}(\mathbf{r})$.

In section 3.2 we assess the amplitudes of individual soft lattice modes in the phase transitions of PTO and PZO. To do so, we use the group symmetry analysis software made available in the ISOTROPY suite, in particular ISODISTORT [60] (6.7.0). This code is able to perform mode decomposition analysis when provided with the cubic $\text{Pm}\bar{3}\text{m}$ parent structures and the distorted daughter structures of PTO and PZO. In our calculations, the parent structures are the relaxed cubic $\text{Pm}\bar{3}\text{m}$ crystals for each basis set and daughter structures are the relaxed ferroelectric tetragonal PTO and antiferroelectric orthorhombic PZO cells for each basis. The soft mode amplitudes can then be extracted from the ionic displacements present in the daughter structures compared with the parents.

2.2. Generation of pseudoatomic orbitals

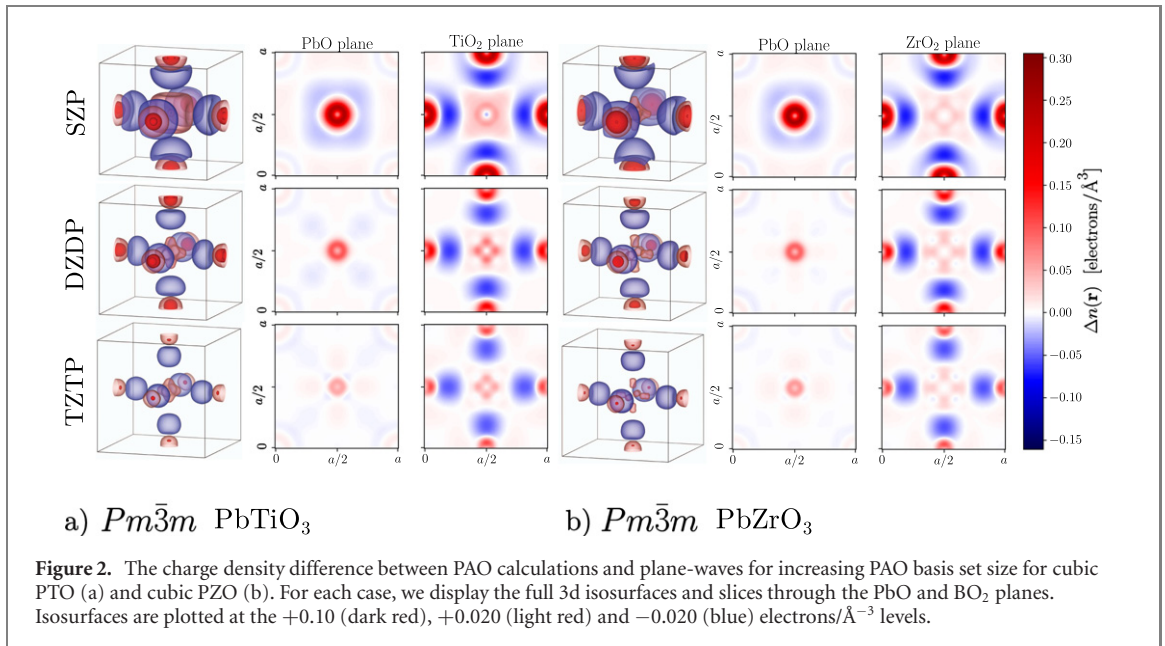
PAOs are a local basis with a simple construction of a radial function $R_{nl\zeta}(\mathbf{r})$ multiplied by an appropriate spherical harmonic $Y_m^l(\hat{\mathbf{r}})$.

$$\chi_{nlm\zeta}(\mathbf{r}) = R_{nl\zeta}(\mathbf{r})Y_m^l(\hat{\mathbf{r}}) \quad (2)$$

for principal quantum number n , orbital angular momentum l and projection of orbital angular momentum m . The last subscript ζ is related to the number of functions per l -channel. Increasing the number of zetas adds flexibility to basis set and improves the accuracy in a non-variational manner. Since the spherical harmonics are analytic functions, the responsibility of the PAO generation code is to solve for the radial functions only. There is a question in this process with regards to how we should apply their confinement. The Siesta code introduced the concept of a uniform energy shift in the eigenvalues of the radial Schrödinger equation. This allows for a consistent definition of confinement for all angular momentum channels across all PAOs. Whilst our approach stems from this, we have implemented two variations for doing so within the CONQUEST PAO generator code (v1.02). One approach is that of *equal energies* where all functions with the same zeta share an energy shift. To increase flexibility of multiple zeta basis sets, one of the zetas should have a large confinement energy to create a highly confined function whilst others should have progressively less confinement. Another approach is *equal radii*. Here, we solve all the radial functions at a given energy shift for given ζ then take the mean of the resulting radii. This radius is then used for the given ζ . It was found in a recent study that whilst both methods showed good agreement with plane-wave calculations, the equal radii approach was found to give slightly better results for lattice constants and bulk moduli versus the equal energies method [33].

Table 1. The cut-off radii r_c for each ζ component of the radial functions which construct the basis sets used in this work by the *equal radii* method. Note that the equal radii method produces radial functions whose cutoff does *not* vary with l -channel. Semi-core states are not included here.

Species	Cut-off radius, r_c (Å)		
	$\zeta = 1$	$\zeta = 2$	$\zeta = 3$
Pb	3.625	2.826	2.000
Zr	4.667	3.551	2.392
Ti	4.355	3.270	2.153
O	2.572	1.979	1.365

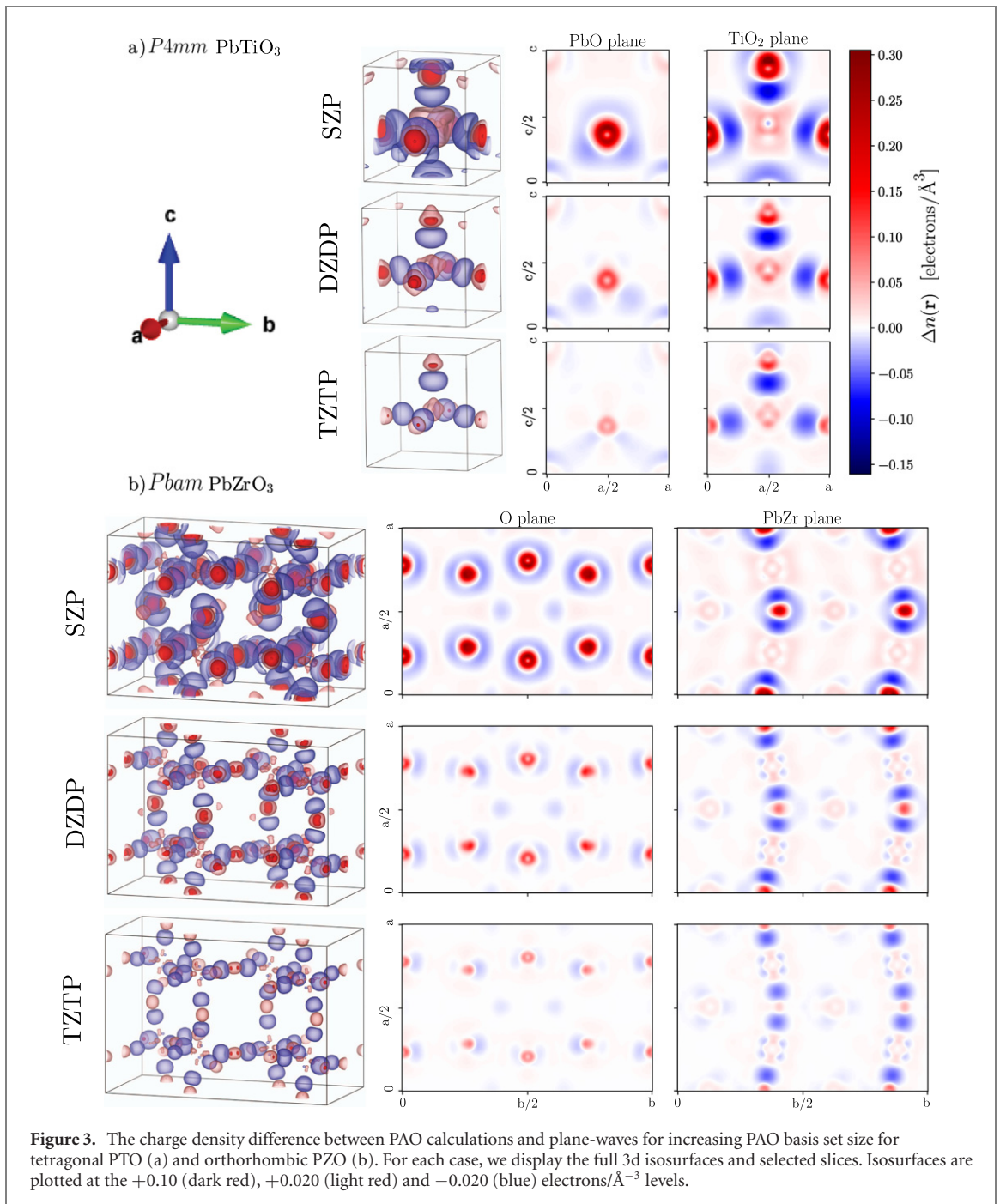


To generate the radial functions for the SZP, DZDP & TZTP basis sets in this study, we use the CONQUEST PAO generator (v1.02) operating under the equal radii scheme. Polarisation functions are solved in a perturbative manner by considering the effect of a finite local electric field acting on the highest valence state [61]. We use the default setting, applying confinement energies of 2 eV, 0.2 eV and 0.02 eV for the first, second and third zetas respectively. The average radii for each zeta for each species for the valence states are shown in table 1. The semi-core Zr and Ti radial functions are highly confined with the Zr 4s & 4p radii being 1.953 Å & 2.281 Å respectively. Ti 3s & 3p semi-core states are cut off at 1.757 Å & 2.001 Å (the radial functions are displayed in section 1 of the supplemental material). The equal radii method produces slightly more compressed functions than the equal energies method which are generally more efficient (due to their smaller cut-off radius) but may require integration on a finer grid due to their more exaggerated gradients. We emphasize once more that the radial functions used in this work are the *defaults* of the PAO generator code. Any results here then should be regarded as *out-of-the-box* performance because in principle, it is possible to fit/optimize these functions for specific situations. For example, the approach made by the *Siesta* code is a downhill simplex minimisation of the total energy carried out on the material system to be studied (usually a solid-state or molecular system) with respect to the parameters of the PAO generation mechanism [24]. Another approach optimises the binding energy curve of dimers [62]. Whilst these methods can produce good results, the possibility of many local minima in the optimisation is an issue as is the overfitting of smaller PAO bases such that their transferability is diminished. In this respect, a large basis set of default (and more general) PAOs may be more transferable.

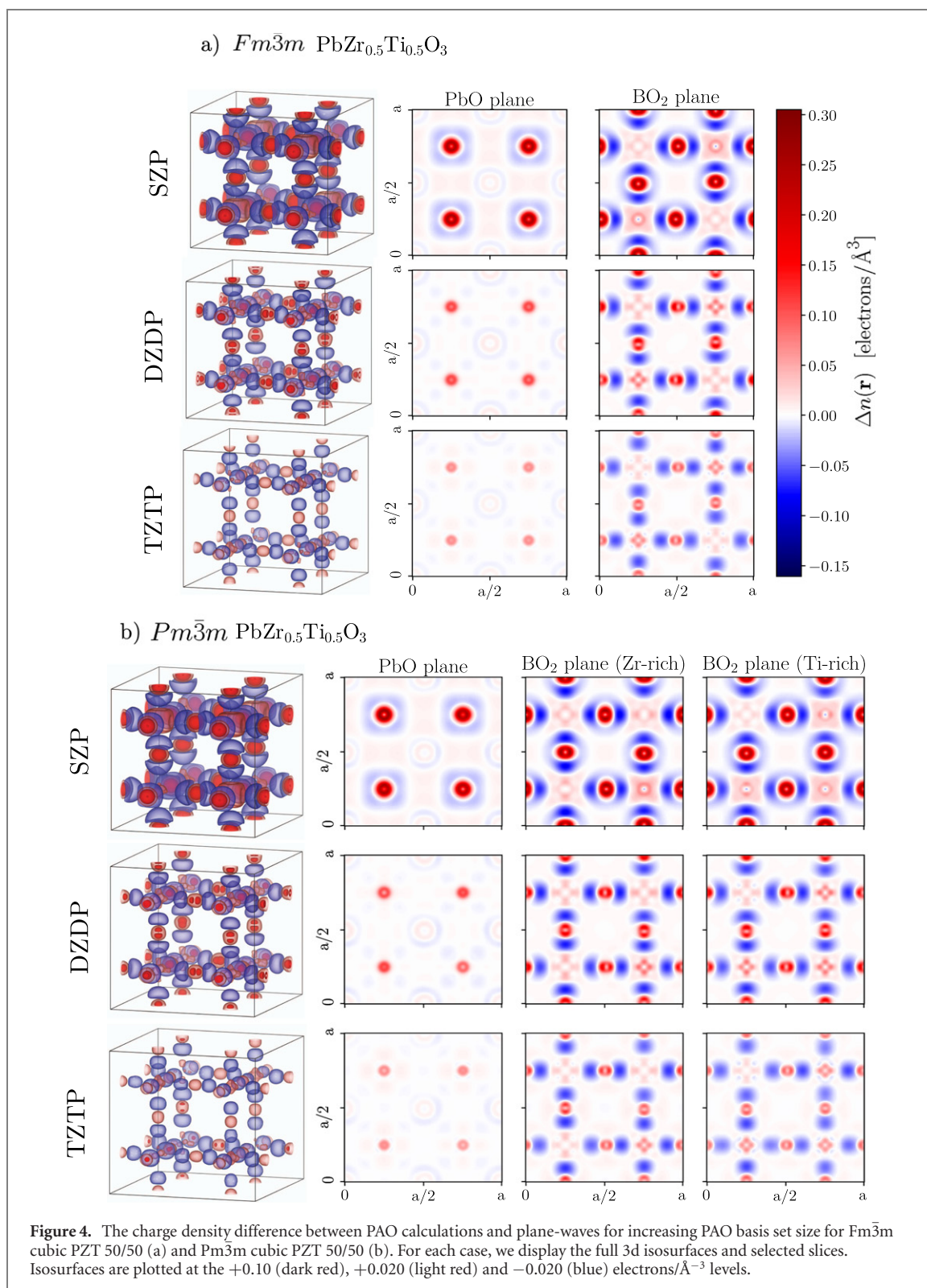
3. Results

3.1. Electronic accuracy

Figures 2–4 show the charge density differences $\Delta n(\mathbf{r}) = n_{\text{PAO}}(\mathbf{r}) - n_{\text{PW}}(\mathbf{r})$ for each PAO basis set and each crystal structure shown in figure 1. We show this quantity using both coloured isosurfaces and slices through



chosen planes which are described in each figure. Before discussing the details of each case, we discuss some striking features shared by all cases. The range of $\Delta n(\mathbf{r})$ is similar between all crystals, extremal at around 0.25 electrons/Å³ with a very narrow region of negative $\Delta n(\mathbf{r})$, minimal at ≈ 0.07 electrons/Å³. Even when considering these extrema, their magnitudes are $\approx 50\times$ smaller than the extrema of any given $n(\mathbf{r})$. This is even more apparent when considering the mean absolute of $\Delta n(\mathbf{r})$ which is ≈ 0.01 electrons/Å³ for SZP falling to ≈ 0.004 electrons/Å³ by TZTP. This shows that even at first glance for all bases the electronic error versus plane-waves is small. It is also clear that these regions of maximal $\Delta n(\mathbf{r})$ are small in volume and isolated close to each ionic site, especially the O anions. Further, error is almost vanishing proximal to the Pb cations and Pb–O bonds suggesting this chemistry is well described by the default PAOs. Other than the aforementioned sites, $\Delta n(\mathbf{r}) \approx 0$ for the vast majority of the simulation box. Since all calculations are normalised to the same number of electrons (44/ABO₃ unit) the localised surplus of electrons close to ionic sites *has to* result in an electron deficiency elsewhere. This manifests itself in two areas. Firstly, a small negative $\Delta n(\mathbf{r})$ appears in bonding areas, especially those characterising the BO₆ octahedra. Secondly, the remaining $\Delta n(\mathbf{r})$ spreads itself out as an even smaller negative background over the rest of the simulation box. Finally, we see



that the effect of increasing the size of the PAO basis from SZP to DZDP results in a large reduction in $\Delta n(\mathbf{r})$. This effect is most clear when we examine the shrinking volumes enclosed by the isosurfaces present on any one of figures 2, 3 or 4. This effect can also be seen as we increase the basis set size from DZDP to TZTP but is less drastic.

Table 2 shows the total integrated electronic error as defined in equation (1). Much like the range of $\Delta n(\mathbf{r})$, the magnitude is similar across all crystals and decreases as we increase the basis set size. This improvement is once again greater between the SZP & DZDP basis sets as compared to the drop in N_{error}^e between DZDP & TZTP. What is notable, however, is that there is a noticeable (but small) gain in N_{error}^e as we break $Pm\bar{3}m$

Table 2. The total integrated electronic error N_{error}^e (normalized per five-atom ABO_3 perovskite unit, containing 44 electrons) as defined in equation (1) for the SZP, DZDP & TZTP PAO basis sets for each of the considered structures in figure 1.

	$N_{\text{error}}^e/\text{ABO}_3$ unit (44 electrons) (e)					
	Pm $\bar{3}$ m		P4mm	Pbam	Fm $\bar{3}$ m	Pm $\bar{3}$ m
	PTO	PZO	PTO	PZO	PZT 50/50	PZT 50/50
SZP	0.719	0.768	0.730	0.772	0.739	0.743
DZDP	0.358	0.382	0.380	0.397	0.369	0.371
TZTP	0.246	0.276	0.257	0.282	0.257	0.259

symmetry for cubic PTO & PZO to the distorted P4mm & Pbam phases respectively. This gain is comparable for both compounds. This effect can be explained by a slight rigidity for each PAO local to sites which become low symmetry. The basis must now adapt to the now distorted environment in a more asymmetrical manner which does not perform as well as the same process at a higher symmetry site. This effect can be seen clearly in figure 3(a) when examining the TiO_2 panel for the SZP basis set. Close to the O 1b Wyck-off site we see firstly that $\Delta n(\mathbf{r})$ is now asymmetrical in the plane perpendicular to the pseudocubic c -axis as compared to the same panel in figure 2(a) where $\Delta n(\mathbf{r})$ is symmetrical. We see also the $\Delta n(\mathbf{r})$ is now greater (and extremal) in the upper region of the O 1b site which is a primary source of the increase in the total integrated error as we break cubic symmetry. We see for the two PZT 50/50 configurations that N_{error}^e is comparable since both arrangements have a similar, cubic symmetry. It is also interesting to point out that the mean of N_{error}^e between cubic PTO & PZO for any basis *very closely* mirrors the value of N_{error}^e for either of the PZT 50/50 configurations. This suggests that the electronic structure local to PTO & PZO units in the alloy is similar to that of the pure compound. This is supported further when examining the BO_2 panels of figure 4 where local PTO & PZO units are easily discernible when compared with the BO_2 panels of figure 2. This suggests that approximations (like the virtual crystal approximation) designed to circumvent the need for large supercell calculations of alloys are unable to accurately account for local electronic structure.

Figure 5(a) quantifies N_{error}^e for Pm $\bar{3}$ m PTO in terms of the same error produced by a given plane-wave cutoff energy using the plane-wave basis. We see that when increasing the number of PAOs to TZTP, we achieve the same accuracy as a 27.28 Ha cutoff plane-wave calculation. Figure 5(b) makes the same comparison but for the convergence of the total energy difference ΔE . All PAO basis sets perform better using this metric (in particular, SZP makes a gain of +4.63 Ha in plane-wave cutoff energy) with TZTP achieving the same convergence in energy as a 30.85 Ha plane-wave cutoff. We note that these values are close to *double* those reported by the PAO basis sets in the *Siesta* code [20] but accept that some of this difference could be accounted for due to the softer (and lower accuracy) Troullier–Martins [63] type pseudopotentials used by the code and the difference in material system used for the study (bulk Si).

Table 3 shows the quantities derived from Bader partitioning of the charge densities calculated using the plane-wave optimised geometries. These results reveal some fine features in the electronic structure. We see that for all basis sets, taking cubic PTO as an example, the Bader ionic charges q_B (obtained from the difference in the pseudopotential valence charge with the Bader partitioned valence charge) *do not* coincide well with the nominal charges (Pb^{2+} , Ti^{4+} , O^{2-}) which are used frequently in the literature as a convenience rather than an *ab initio* assignment. We retrieve around half the nominal values suggesting a significant covalent character to the bonding, especially for the BO_6 octahedra. This is in contrast to the well known phenomenon of anomalous dynamical or *Born effective charges* (\mathbf{Z}^*) in the perovskite oxides, known to approximately *double* the nominal charges of ions in the perovskite oxides [64]. The reason for this discrepancy is that the dynamical nature of \mathbf{Z}^* accounts for the additional charge from counter motion of electrons/holes when an cation/anion is displaced. In comparison, the Bader charge calculated in this work is a static property.

We see that there is a cation \rightarrow anion negative charge transfer with increasing basis set size suggesting an increasing level of ionicity in bonding bringing q_B closer to their nominal values. We see that the prediction of q_B is rather underestimated for cations and overestimated for anions in the SZP basis set. This suggests that the electronegativity of O is underestimated and/or electrons on the metal ion sites are over-localised compared to plane-waves. This fact first appears to be at odds with the observed effect of an electron surplus near O anions as seen in figures 2–4. This is however rationalised as we also observe a decrease in the Bader volume V_B for O anions which, in turn, increases the average valence charge density \bar{n}_B (as seen in table 3) recovering the effect observed in the electron density difference plots. Whilst it can be seen that the Bader derived quantities are rather approximate (most notably in q_B) for the SZP basis, by DZDP (and *certainly* by TZTP) they

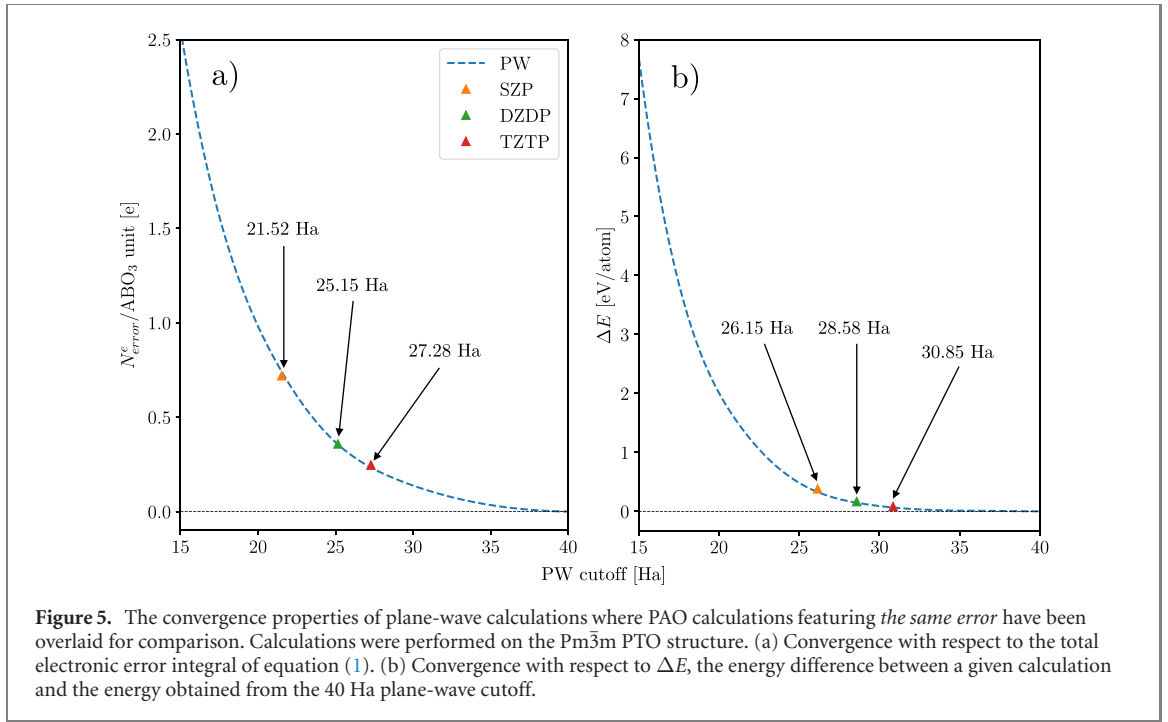


Figure 5. The convergence properties of plane-wave calculations where PAO calculations featuring *the same error* have been overlaid for comparison. Calculations were performed on the $\text{Pm}\bar{3}\text{m}$ PTO structure. (a) Convergence with respect to the total electronic error integral of equation (1). (b) Convergence with respect to ΔE , the energy difference between a given calculation and the energy obtained from the 40 Ha plane-wave cutoff.

are in good agreement with the values obtained from plane-waves. This once again emphasizes the electronic accuracy achievable with the default PAOs.

We have also examined the possibility that the errors in q_B could be an artefact of pressure using the particular case of $\text{Pm}\bar{3}\text{m}$ PZO. We can see from table 6 that the optimised lattice constants for the PAO bases overestimate the plane-wave result by 0.99%, 0.46% and 0.34% for the SZP, DZDP and TZTP basis sets respectively. If we then perform simulations at the plane-wave lattice constant (as was done for the results in table 3) this imposes an isotropic pressure of -5.28 GPa (SZP), -2.63 GPa (DZDP) and -1.46 GPa (TZTP). Because of this fact, we calculated the Bader quantities once more using the zero pressure lattice constants. Remarkably, q_B changes only marginally (no more than $\pm 0.01e$). Since we are working at a larger volume, the V_B must of course increase, but, the ratios of the cationic to anionic volumes remain constant. Since roughly the same amount of charge is now enclosed within a larger V_B , we naturally see a decreased \bar{n}_B for all sites.

We see that the ratio of the cation to anion volumes is a decreasing function of basis set completeness, decreasing by ≈ 0.1 for V_B^B/V_B^O and ≈ 0.2 for V_B^{Pb}/V_B^O from SZP to TZTP. This implies that in the smaller basis set, O occupies a smaller ionic volume in comparison to the Pb and B-sites. This could result in small differences in lattice dynamics between the basis sets and could effect the Goldschmidt tolerance factor, depending explicitly on ionic radii [65, 66].

3.2. Soft-mode distortions

In this section we consider the soft-modes known to drive the phase transitions in PTO and PZO. We consider the amplitude of each identifiable irrep in the relaxed structures for each basis set. We also consider the degree of energy lowering associated with each of these irreps and define phase transition energies. We display the displacive modes in tables 4 and 5. Strain modes influence the phase transition in PZO only by a small amount so we include only discussion of strain modes in PTO, coupling strongly to the displacive Γ_4^- mode. The phase transition energies are quoted in table 7 and the linear evolution of mode energetics are shown in figure 6.

Before discussing mode amplitudes, we must first carefully define them. We do so following the format of the ISODISTORT A_p amplitude normalised to the primitive cell [60]. Once an atomic displacement has been identified as belonging to a particular irrep, the displacement is calculated in fractional coordinates relative to the *parent* structure. This defines the amplitude of a specific displacement in the irrep. To calculate A_p we now normalise the amplitude by a factor of $\sqrt{V_p/V_s}$ for supercell/primitive cell volumes $V_{p/s}$. Now to calculate the amplitude of the irrep as a whole, we take the square root of the sum of the squares of the displacement amplitudes belonging to the irrep in question (thereby obtaining an RMS amplitude). If we wish to characterise the amplitude of the total distortion from the transition, we can take the square root of the sum of the squares for each irrep amplitude. Tables 4 and 5 are then tabulations of A_p .

Table 3. The Bader partitioned ionic charges q_B , volumes V_B and average valence charge densities \bar{n}_B for each ionic species and each of the considered crystal structures calculated for each basis set. Where ionic species have symmetry in-equivalent sites, we take the mean value over all sites. We give also the mean relative error (MRE) ϵ and mean absolute relative error (MARE) ϵ^{abs} measured in % error versus plane-waves.

	q_B (e)				V_B (\AA^3)				\bar{n}_B ($\text{e}\text{\AA}^{-3}$)			
	SZP	DZDP	TZTP	PW	SZP	DZDP	TZTP	PW	SZP	DZDP	TZTP	PW
Pm $\bar{3}$ m PTO												
Pb	1.29	1.37	1.39	1.38	18.81	18.40	18.39	18.41	0.676	0.686	0.686	0.686
Ti	2.01	2.08	2.12	2.15	7.68	7.54	7.42	7.35	1.300	1.315	1.331	1.344
O	-1.10	-1.15	-1.17	-1.18	11.22	11.40	11.45	11.46	0.633	0.627	0.6326	0.626
Pm $\bar{3}$ m PZO												
Pb	1.21	1.30	1.39	1.35	21.89	21.42	20.83	21.06	0.585	0.593	0.606	0.600
Zr	2.31	2.39	2.43	2.47	11.00	10.65	10.39	10.23	0.881	0.903	0.921	0.931
O	-1.17	-1.23	-1.27	-1.27	12.70	12.97	13.25	13.23	0.565	0.557	0.549	0.550
P4mm PTO												
Pb	1.27	1.35	1.39	1.37	19.70	19.26	19.07	19.16	0.646	0.657	0.661	0.659
Ti	2.03	2.10	2.13	2.16	7.83	7.67	7.56	7.48	1.273	1.291	1.306	1.315
O	-1.10	-1.15	-1.17	-1.18	11.76	11.96	12.07	12.06	0.603	0.597	0.594	0.595
Pbam PZO												
Pb	1.20	1.29	1.34	1.31	21.24	20.70	20.52	20.66	0.603	0.614	0.617	0.614
Zr	2.37	2.47	2.51	2.55	10.99	10.61	10.39	10.28	0.876	0.898	0.913	0.920
O	-1.19	-1.25	-1.28	-1.29	12.79	13.10	13.23	13.22	0.562	0.554	0.550	0.551
Fm $\bar{3}$ m PZT 50/50												
Pb	1.24	1.34	1.39	1.35	20.29	19.78	19.52	19.76	0.629	0.640	0.646	0.640
Zr	2.26	2.36	2.42	2.55	10.91	10.54	10.28	9.96	0.892	0.915	0.933	0.949
Ti	2.04	2.12	2.15	2.18	7.70	7.53	7.43	7.34	1.294	1.313	1.325	1.338
O	-1.13	-1.19	-1.22	-1.24	11.87	12.13	12.28	12.27	0.601	0.593	0.588	0.590
Pm $\bar{3}$ m PZT 50/50												
Pb	1.24	1.34	1.39	1.36	20.45	19.86	19.60	19.79	0.624	0.637	0.643	0.639
Zr	2.33	2.39	2.43	2.47	10.64	10.43	10.18	10.03	0.909	0.921	0.939	0.950
Ti	2.04	2.11	2.15	2.18	7.73	7.54	7.42	7.34	1.289	1.311	1.327	1.337
O	-1.14	-1.20	-1.23	-1.23	12.01	12.27	12.42	12.39	0.595	0.587	0.582	0.583
ϵ (%)	-7.55	-2.83	-0.26	—	2.45	1.20	0.37	—	-1.73	-0.89	-0.26	—
ϵ^{abs} (%)	7.55	2.83	1.45	—	4.27	1.84	4.27	—	2.82	1.25	0.60	—

We consider first the simpler phase transition of PTO. This is characterised by a single displacive mode Γ_4^- resulting in the ferroelectric P4mm phase. Examining table 4 we see that Pb 1b displacements are set to zero since we have chosen the Pb site as the origin. We see that for the SZP basis set the Γ_4^- distortion is rather approximate compared to plane-waves overestimated by $\approx 35\%$. This overestimate can be understood in simple terms by considering the arguments of Cochran and Anderson [37, 38, 67] in their seminal works on soft modes. It is suggested that the condition for stability against the ferroelectric distortion is that short range restoring forces (favouring the cubic phase) outweigh long range Coulombic forces (favouring ferroelectricity). This condition does not hold for PTO in 0K DFT hence the ferroelectric Γ_4^- mode is an energy lowering phase transition of the Pm $\bar{3}$ m phase. It is clear, however, that this delicate balance of short and long range forces is modified between the different PAO bases. As discussed in section 1 (and displayed in figure 2(a)), there are too few electrons in the covalent bonds defining the TiO_6 octahedra; an effect especially apparent for the SZP basis. This reduces the strength of short range restoring forces whilst the Coulombic Ewald contribution remains constant (since for these calculations, we work at the plane-wave lattice constant for each basis). We suggest that this increased imbalance drives a much stronger ferroelectric distortion for the SZP basis. We note that whilst the Hartree forces (a functional of the charge density) from the coulomb interacting electrons will also play a role in this balancing act, their contribution is non-trivial.

Table 4. The mode amplitudes normalised to the parent cell A_p (described in the text) for the irreps characterising the $Pm\bar{3}m \rightarrow P4mm$ phase transition in PTO.

			SZP	DZDP	TZTP	PW
$\Gamma_4^- \rightarrow \mathbf{q}_\Gamma = [0, 0, 0]$	Pb 1b	T_{1u}	0.000	0.000	0.000	0.000
	Ti 1a	T_{1u}	0.160	0.118	0.111	0.141
	O 3d	A_{2u}	0.659	0.458	0.370	0.446
	O 3d	E_u	0.842	0.646	0.550	0.651
	Total distortion			1.081	0.800	0.672

Table 5. The mode amplitudes normalised to the parent cell A_p (described in the text) for the irreps characterising the $Pm\bar{3}m \rightarrow Pbam$ phase transition in PZO. The modes are listed in descending total distortion.

			SZP	DZDP	TZTP	PW
$R_4^+ \rightarrow \mathbf{q}_R = [1/2, 1/2, 1/2]$	O 3d	E_u	0.571	0.554	0.553	0.534
	Total R_4^+ distortion		0.571	0.554	0.553	0.534
$\Sigma_2 \rightarrow \mathbf{q}_\Sigma = [1/4, 1/4, 0]$	Pb 1b	T_{1u}	0.213	0.214	0.239	0.256
	Zr 1a	T_{1u}	0.041	0.034	0.037	0.047
	O 3d	A_{2u}	-0.047	-0.042	-0.035	-0.035
	O 3d	E_{u_1}	0.253	0.250	0.224	0.227
	O 3d	E_{u_2}	-0.230	-0.222	-0.216	-0.217
	Total Σ_2 distortion			0.407	0.400	0.396
$S_4 \rightarrow \mathbf{q}_S = [1/4, 1/2, 1/4]$	Pb 1b	T_{1u}	-0.049	-0.033	-0.026	-0.026
	O 3d	E_{u_1}	-0.013	-0.129	-0.103	-0.106
	O 3d	E_{u_2}	0.074	-0.083	-0.071	-0.070
	Total S_4 distortion			0.154	0.157	0.128
$M_5^- \rightarrow \mathbf{q}_M = [1/2, 1/2, 0]$	Pb 1b	T_{1u}	-0.006	-0.001	-0.009	-0.010
	Zr 1a	T_{1u}	-0.008	-0.003	-0.006	-0.008
	O 3d	E_u	0.012	0.013	0.009	0.009
	Total M_5^- distortion			0.015	0.013	0.014
$R_5^+ \rightarrow \mathbf{q}_R = [1/2, 1/2, 1/2]$	Pb 1b	T_{1u}	0.011	0.024	0.027	0.027
	O 3d	E_u	-0.001	-0.006	-0.007	0.008
	Total R_5^+ distortion			0.011	0.025	0.028
$X_3^- \rightarrow \mathbf{q}_X = [0, 1/2, 0]$	Zr 1a	T_{1u}	0.001	0.0003	0.002	0.003
	O 3d	E_u	-0.009	-0.009	-0.017	-0.017
	Total X_3^- distortion			0.009	0.009	0.018
Overall distortion			0.718	0.702	0.693	0.686

Consider also the coupling to strain modes $\Gamma_{1\sigma}^+$ and $\Gamma_{3\sigma}^+$ (the subscript σ denotes a strain mode rather than a displacive one). The former is responsible for uniform isotropic expansions/contractions of the cell whilst the latter is responsible for tetragonality. Rather than quote the amplitude of each mode for each basis (which is available in the supplementary material), it is more illuminating to examine the zero pressure lattice constants of table 6. We see that for the SZP basis the c/a ratio is considerably overestimated at 1.24 when compared to the plane-wave c/a of 1.084. This implies also a considerable overestimate of the amplitudes of $\Gamma_{1\sigma}^+$ and $\Gamma_{3\sigma}^+$. The amplitude of the ferroelectric Γ_4^- distortion is then increased as a result of the strong, mutual coupling to $\Gamma_{1\sigma}^+$ and $\Gamma_{3\sigma}^+$. A peculiarity of this transition for the default PAOs is their non-systematic nature. Despite the smaller number of basis functions, the DZDP basis performs better than TZTP for the amplitude of displacive modes, strain modes, the phase transition energy (table 7) and lattice constants of the $P4mm$ phase (table 6). It is for this reason that great care must be taken when using PAOs to describe systems where the internal and cell degrees of freedom are strongly coupled. We note that using a basis other than the default can result in vast improvements for this transition. When tuning the confinement energies to fit the plane-wave c/a , we can achieve a phase transition energy within 1 meV of the plane-wave energy (shown in the supplemental material).

We have also computed the spontaneous macroscopic polarisation for the relaxed $P4mm$ PTO structures. For the PAO calculations, we use the method developed by Resta [68, 69] (equivalent to the Berry phase formalism [70, 71] in the limit of large cells; we use ten cells in the direction of the distortion) whilst we use the well known Berry phase formalism of King-Smith and Vanderbilt for the plane-wave calculation. With plane-waves, we find a polarisation of $92.74 \mu\text{Ccm}^{-2}$ which compares very well with the

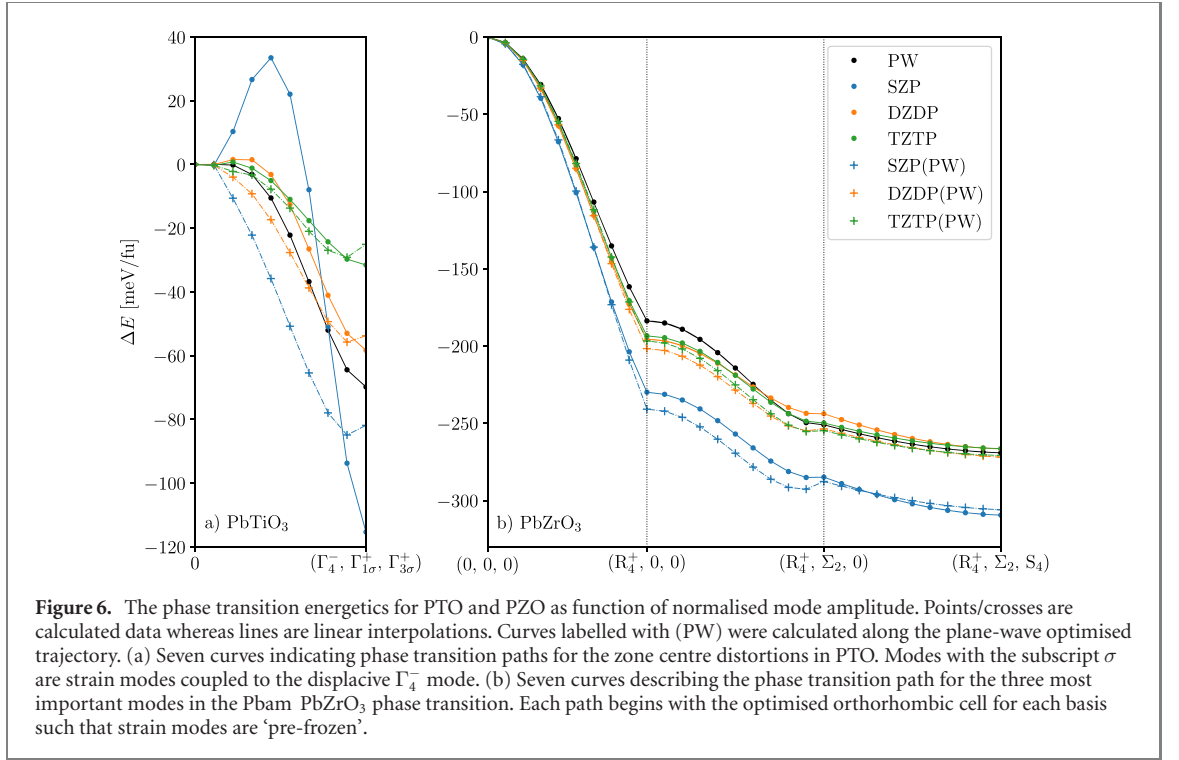


Table 6. The optimised, mutually orthogonal, pseudocubic lattice constants a , b and c for each of the considered crystals and basis set.

	SZP (Å)			DZDP (Å)			TZTP (Å)			PW (Å)		
	a	b	c	a	b	c	a	b	c	a	b	c
Pm $\bar{3}m$ PTO	3.952	3.952	3.952	3.928	3.928	3.928	3.926	3.926	3.926	3.918	3.918	3.918
Pm $\bar{3}m$ PZO	4.181	4.181	4.181	4.159	4.159	4.159	4.154	4.154	4.154	4.140	4.140	4.140
P4mm PTO	3.799	3.799	4.710	3.865	3.865	4.282	3.890	3.890	4.128	3.870	3.870	4.194
Pbam PZO	5.919	11.907	8.241	5.877	11.835	8.223	5.886	11.793	8.206	5.871	11.765	8.178
Fm $\bar{3}m$ PZT 50/50	8.124	8.124	8.124	8.091	8.091	8.091	8.080	8.080	8.080	8.050	8.050	8.050
Pm $\bar{3}m$ PZT 50/50	8.143	8.143	8.143	8.112	8.112	8.112	8.096	8.096	8.096	8.069	8.069	8.069

Table 7. The phase transition energies for the cubic to tetragonal/orthorhombic transitions in PTO/PZO. This quantity is defined by the difference in total energy between the relaxed cubic phase and the relaxed distorted phase for each basis.

	PTO Pm $\bar{3}m$ \Rightarrow P4mm (meV/ABO ₃ unit)	PZO Pm $\bar{3}m$ \Rightarrow Pbam (meV/ABO ₃ unit)
SZP	-115.51	-295.78
DZDP	-58.40	-256.27
TZTP	-47.37	-258.71
PW	-69.83	-262.24

TZTP value of $92.82 \mu\text{Ccm}^{-2}$. We note that this is despite the underestimation of the displacive Γ_4^- mode (indicative of the ionic contribution, table 4) meaning the electronic contribution to the polarisation is increased. The DZDP polarisation is found to be $104.15 \mu\text{Ccm}^{-2}$ showing that despite the Γ_4^- mode amplitude closely adhering to the plane-wave value, the electronic contribution is slightly overestimated. For the SZP basis, we find a polarisation of $95.93 \mu\text{Ccm}^{-2}$ which at first glance indicates better agreement with plane-waves than DZDP. We note that this is only because the significantly larger dipole moment (as indicated by the mode amplitude in table 4) is normalised by the largely overestimated volume (+8.2% compared to plane-waves).

The PZO transition is more difficult to unpack. Despite this, (perhaps due to only a weak coupling between displacive and strain modes) the material is impressively described by the default PAOs. The error in both

the $\text{Pm}\bar{3}\text{m}$ and Pbam lattice constants are smaller than 0.5% for the TZTP basis demonstrating that even highly distorted perovskites can be represented well by the default PAOs. We now examine table 5 commenting on the individual contributions of each irrep in the transition. Beginning first with the R_4^+ mode we see that the accuracy improves with basis set size but accounts for the largest source of error in the overall distortion. Since the R_4^+ mode is AFD, this overestimation leads to a larger rotation angle of the oxygen octahedra compared to plane-waves. For the antipolar Σ_2 distortion, we see that the total distortion becomes *further* from the plane-wave value as we increase the number of basis functions. This is somewhat misleading however as when we examine the individual displacements, we see that O and Pb displacements are better described by the TZTP basis. The reason the SZP basis *appears* to perform better is because the underestimated Pb displacement balances with the O E_{u_2} displacement. Taking both the S_4 and X_3^- modes together, we see that an accurate description requires the TZTP basis. It should be noted, however, the X_3^- mode contributes very little to the energetics of the transition which is dominated by the R_4^+ , Σ_2 and S_4 modes. We note finally that although the amplitudes of some modes does not improve with basis set size, the overall distortion does. By TZTP, the distortion is within 0.1% of the plane-wave distortion. This accuracy is seen also in the phase transition energy (table 7) which improves with basis set size within 1% of the plane-wave value by TZTP.

Figure 6 describes the energy difference ΔE between an initial, undistorted phase and a phase distorted by some fraction of a displacive or strain mode. For each basis, the maximum amplitude of an irrep is the amplitude found in the relaxed structure in tables 4 and 5. In figure 6(a), the initial undistorted structure is the optimised $\text{Pm}\bar{3}\text{m}$ PTO structure for the basis in question. Since the displacive mode is coupled strongly to the strain modes, we linearly evolve the three modes (Γ_4^- , $\Gamma_{1\sigma}^+$ and $\Gamma_{3\sigma}^+$) simultaneously until their maximum amplitudes are reached. As was explained previously, the default DZDP basis best approximates the plane-wave energetics since the TZTP basis retrieves a less accurate c/a ratio. A small energy barrier (at zero mode amplitude) exists for the transition for *all* cases. This is not true in reality, only existing here since we have assumed the displacive and strain modes are directly proportional on a 1:1 basis (the real coupling is non-linear). Notable however, is the size of the barrier for the SZP basis of ≈ 35 meV. This is an artefact of the large strain modes and the highly non-linear coupling with the displacive mode. For curves along the plane-wave optimised trajectory (explained in the figure 6 caption), a minimum of energy is always reached before the mode maximum inferring that the optimised plane-wave structure does not so well approximate the optimised structure of a given PAO basis. This, much like the phase transition energy, can be improved upon using a non-default basis.

In figure 6(b), our initial undistorted structure is the optimised orthorhombic Pbam cell of PZO (with lattice constants described in table 6) but with *zero* displacive mode amplitude. As a general trend, we see that there is a fair discrepancy between the SZP and plane-wave curves. This almost disappears as we use a DZDP basis and even more so by TZTP. A clear source of error in our description for all bases is the overestimated amplitude the R_4^+ mode. We see that along the $(0, 0, 0) \rightarrow (\text{R}_4^+, 0, 0)$ path, this overestimation results in *too much* energy lowering. Interestingly, for the DZDP and TZTP bases, this error seems to recover along the $(\text{R}_4^+, 0, 0) \rightarrow (\text{R}_4^+, \Sigma_2, 0)$ path and by the time all three displacive modes are present, the energetics are almost identical. For the plane-wave optimised trajectories, we once again observe a minimum of energy before the maximal mode amplitude. This barrier appears just before the $(\text{R}_4^+, \Sigma_2, 0)$ point indicating that the plane-wave Σ_2 mode (when coupled to R_4^+ at least) does not describe a stable structure. This effect does appear to diminish with basis set size, disappearing almost entirely for TZTP. At the (final) $(\text{R}_4^+, \Sigma_2, \text{S}_4)$ point, we see that the DZDP, DZDP(PW), TZTP and TZTP(PW) curves very well represent the PW curve. This implies that in this case, the default PAOs could be used to describe a plane-wave optimised structure with only a very small penalty in the energetics. This is valuable since this allows us take small plane-wave optimised cells to build larger supercells for PAO calculations *without re-relaxing* the structure allowing for easy up-scaling of accurate DFT calculations.

4. Summary

We have investigated the consequences of representing delicate features of the perovskite oxides with the default CONQUEST basis sets of PAOs as a replacement for plane-waves. In the electronic structure, we were able to reproduce the plane-wave electronic charge density with an error of $\approx 0.5\%$ using the total integrated electronic error integral of equation (1). We found that the largest source of error to this integral is from a surplus of electronic density close to O anion sites as shown in electronic charge density difference plots. Even fine features derived from Bader partitioning (Bader charges, volumes and densities) agree well with plane-wave calculations and once again demonstrates the small surplus in electronic density near

O anion sites. We quantified the completeness of the PAO basis sets by providing plane-wave cutoff energies offering the same accuracy in N_{error} and energy convergence as those using the plane-wave basis. We found that although the two metrics disagree (by a small amount) on the cutoff, by TZTP we can achieve the accuracy of a 27.28–30.85 Ha plane-wave cutoff, close to *double* what has previously been reported in the literature. We note that whilst this comparison is useful, the error cancellation in the plane-wave basis (that is, error in the core regions tend to cancel with one another) is not perfectly achieved when we consider the energy difference between plane-wave and PAO calculations. Further, we do not expect these errors to be system dependent in the case of plane-waves but could be for PAOs, especially smaller basis sets (like SZ and SZP).

When investigating the condensation of soft-modes, we found that larger basis sets of PAOs (DZDP and TZTP) well described the $\text{Pm}\bar{3}\text{m} \rightarrow \text{Pbam}$ phase transition in PZO, both structurally and energetically. Impressively, both the total distortion and phase transition energy when using the TZTP basis is within 1% of the plane-wave figures. We found that more care had to be taken for the $\text{Pm}\bar{3}\text{m} \rightarrow \text{P4mm}$ phase transition in PTO due to the strong coupling between displacive and strain modes. This, however, can be remedied by using a non-default optimised basis. Remarkably, we find that using a default DZDP or TZTP basis set on a plane-wave optimised geometry for PZO results in close to identical phase transition energies. This suggests that even highly distorted perovskites can be represented by basis sets of default PAOs.


This work suggests that even fine structural and electronic features of the perovskite oxides can be calculated to near plane-wave accuracy using basis sets of PAOs. Since PAO-based calculations (in partnership with the correct algorithm) can scale to many thousands (and millions [31]) of atoms, this approach now offers a pathway for accurate large scale first principles simulations of perovskite systems using DFT. We note that whilst there is still progress to be made for the calculation of more demanding physical properties (like soft mode phase transition temperatures), some particularly valuable research questions (as discussed in section 1) facing the perovskite oxides can now be addressed with this method using large scale structural relaxations, spin-polarised calculations with highly disordered magnetism and the extraction of electronic properties from systems with realistic defect concentrations.

Acknowledgments

The authors are grateful for computational support from the UK Materials and Molecular Modelling Hub, which is partially funded by EPSRC (EP/P020194), for which access was obtained via the UKCP consortium and funded by EPSRC Grant ref EP/P022561/1. We are also thankful for the computational resources provided by the London Centre for Nanotechnology, including access to the Salviati computing cluster. We thank Kane Shenton for useful discussions and for his implementation of Resta's method [68] for the calculation of the macroscopic polarisation.

ORCID iDs

Jack S Baker  <https://orcid.org/0000-0001-6635-1397>

Tsuyoshi Miyazaki  <https://orcid.org/0000-0003-3534-4404>

David R Bowler  <https://orcid.org/0000-0001-7853-1520>

References

- [1] Hwang H Y, Iwasa Y, Kawasaki M, Keimer B, Nagaosa N and Tokura Y 2012 Emergent phenomena at oxide interfaces *Nat. Mater.* **11** 103–13
- [2] Huijben M, Brinkman A, Koster G, Rijnders G, Hilgenkamp H and Blank D H A 2009 Structure-property relation of $\text{SrTiO}_3/\text{LaAlO}_3$ interfaces *Adv. Mater.* **21** 1665–77
- [3] Zubko P, Wojdeł J C, Hadjimichael M, Fernandez-Pena S, Sené A, Luk'yanchuk I, Triscone J-M and Íñiguez J 2016 Negative capacitance in multidomain ferroelectric superlattices *Nature* **534** 524–8
- [4] Mora-Seró I, Bisquert J, Fabregat-Santiago F, Garcia-Belmonte G, Zoppi G, Durose K, Proskuryakov Y, Oja I, Belaidi A *et al* 2006 Implications of the negative capacitance observed at forward bias in nanocomposite and polycrystalline solar cells *Nano Lett.* **6** 640–50
- [5] Maeno Y, Hashimoto H, Yoshida K, Nishizaki S, Fujita T, Bednorz J G and Lichtenberg F 1994 Superconductivity in a layered perovskite without copper *Nature* **372** 532–4
- [6] Xiao G, Cieplak M Z, Gavrin A, Streitz F H, Bakhshai A and Chien C L 1988 High-temperature superconductivity in tetragonal perovskite structures: is oxygen-vacancy order important? *Phys. Rev. Lett.* **60** 1446–9
- [7] Gareeva Z V and Zvezdin A K 2009 Interacting antiferromagnetic and ferroelectric domain structures of multiferroics *Phys. Status Solidi* **3** 79–81

- [8] Benedek N A and Fennie C J 2011 Hybrid improper ferroelectricity: a mechanism for controllable polarization–magnetization coupling *Phys. Rev. Lett.* **106** 107204
- [9] Spaldin N A and Ramesh R Feb. 2019 Advances in magnetoelectric multiferroics *Nat. Mater.* **18** 203–12
- [10] Streiffer S K, Eastman J A, Fong D D, Thompson C, Munkholm A, Murty M V R, Auciello O, Bai G R and Stephenson G B 2002 Observation of nanoscale 180° stripe domains in ferroelectric PbTiO₃ thin films *Phys. Rev. Lett.* **89** 067601
- [11] Fong D D 2004 Ferroelectricity in ultrathin perovskite films *Science* **304** 1650–3
- [12] Sosnowska I, Neumaier T P and Steichele E 1982 Spiral magnetic ordering in bismuth ferrite *J. Phys. C: Solid State Phys.* **15** 4835–46
- [13] Burns S R et al 2019 Expansion of the spin cycloid in multiferroic BiFeO₃ thin films *npj Quantum Mater.* **4** 18
- [14] Baker J S and Bowler D R 2019 First-principles soft-mode lattice dynamics of PbZr_{0.5}Ti_{0.5}O₃ and shortcomings of the virtual crystal approximation *Phys. Rev. B* **100** 224305
- [15] Bellaïche L and Vanderbilt D 2000 Virtual crystal approximation revisited: application to dielectric and piezoelectric properties of perovskites *Phys. Rev. B* **61** 7877–82
- [16] Ramer N J and Rappe A M 2000 Virtual-crystal approximation that works: locating a compositional phase boundary in PbZr_{1-x}Ti_xO₃ *Phys. Rev. B* **62** R743
- [17] Singh D J and Nordstrom L 2006 *Planewaves, Pseudopotentials, and the LAPW Method* (Berlin: Springer) (<https://doi.org/10.1007/978-0-387-29684-5>)
- [18] Lejaeghere K et al 2016 Reproducibility in density functional theory calculations of solids *Science* **351** aad3000
- [19] Kenny S, Horsfield A and Fujitani H 2000 Transferable atomic-type orbital basis sets for solids *Phys. Rev. B* **62** 4899–905
- [20] Soler J M, Artacho E, Gale J D, García A, Junquera J, Ordejón P and Sánchez-Portal D 2002 The SIESTA method for *ab initio* order-*N* materials simulation *J. Phys.: Condens. Matter.* **14** 2745–79
- [21] Sankey O F and Niklewski D J 1989 *Ab initio* multicenter tight-binding model for molecular-dynamics simulations and other applications in covalent systems *Phys. Rev. B* **40** 3979
- [22] Torralba A, Todorović M, Brázdová V, Choudhury R, Miyazaki T, Gillan M and Bowler D 2008 Pseudo-atomic orbitals as basis sets for the $\mathcal{O}(N)$ DFT code CONQUEST *J. Phys.: Condens. Matter.* **20** 294206
- [23] Louwse M J and Rothenberg G 2012 Transferable basis sets of numerical atomic orbitals *Phys. Rev. B* **85** 035108
- [24] Junquera J, Paz Ó, Sánchez-Portal D and Artacho E 2001 Numerical atomic orbitals for linear-scaling calculations *Phys. Rev. B* **64** 23511
- [25] Anglada E, Soler J M, Junquera J and Artacho E 2002 Systematic generation of finite-range atomic basis sets for linear-scaling calculations *Phys. Rev. B* **66** 205101
- [26] Ozaki T 2003 Variationally optimized atomic orbitals for large-scale electronic structures *Phys. Rev. B* **67** 155108
- [27] Bowler D R, Choudhury R, Gillan M J and Miyazaki T 2006 Recent progress with large-scale *ab initio* calculations: the CONQUEST code *Phys. Status Solidi b* **243** 989–1000
- [28] Bowler D, Miyazaki T and Gillan M 2001 Parallel sparse matrix multiplication for linear scaling electronic structure calculations *Comput. Phys. Commun.* **137** 255–73
- [29] Kohn W 1996 Density functional and density matrix method scaling linearly with the number of atoms *Phys. Rev. Lett.* **76** 3168–71
- [30] Bowler D and Miyazaki T 2012 $\mathcal{O}(N)$ methods in electronic structure calculations *Rep. Prog. Phys.* **75** 036503
- [31] Bowler D R and Miyazaki T 2010 Calculations for millions of atoms with density functional theory: linear scaling shows its potential *J. Phys.: Condens. Matter.* **22** 074207
- [32] Bowler D R et al 2020 The CONQUEST code: public release <https://github.com/OrderN/CONQUEST-release>
- [33] Bowler D R, Baker J S, Poulton J T L, Mujahed S Y, Lin J, Yadav S, Raza Z and Miyazaki T 2019 Highly accurate local basis sets for large-scale DFT calculations in CONQUEST *Japan. J. Appl. Phys.* **58** 100503
- [34] Lee K, Yu J and Morikawa Y 2007 Comparison of localized basis and plane-wave basis for density-functional calculations of organic molecules on metals *Phys. Rev. B* **75** 045402
- [35] Otsuka T, Miyazaki T, Ohno T, Bowler D R and Gillan M J 2008 Accuracy of order-*N* density-functional theory calculations on DNA systems using CONQUEST *J. Phys.: Condens. Matter.* **20** 294201
- [36] Yin B, Aguado-Puente P, Qu S and Artacho E 2015 Two-dimensional electron gas at the PbTiO₃/SrTiO₃ interface: an *ab initio* study *Phys. Rev. B* **92** 115406
- [37] Cochran W 1959 Crystal stability and the theory of ferroelectricity *Phys. Rev. Lett.* **3** 412–4
- [38] Cochran W 1960 Crystal stability and the theory of ferroelectricity *Adv. Phys.* **9** 387–423
- [39] Howard S T and Lamarche O 2003 Description of covalent bond orders using the charge density topology *J. Phys. Org. Chem.* **16** 133–41
- [40] Zhang L, Ying F, Wu W, Hiberty P and Shaik S 2009 Topology of electron charge density for chemical bonds from valence bond theory: a probe of bonding types *Chem. Eur. J.* **15** 2979–89
- [41] Martin R M 2004 *Electronic Structure: Basic Theory and Practical Methods* (Cambridge: Cambridge University Press)
- [42] Nelmes R and Kuhs W 1985 The crystal structure of tetragonal PbTiO₃ at room temperature and at 700 K *Solid State Commun.* **54** 721–3
- [43] Tagantsev A K et al 2013 The origin of antiferroelectricity in PbZrO₃ *Nat. Commun.* **4** 2229
- [44] Mani B K, Lisenkov S and Ponomareva I 2015 Finite-temperature properties of antiferroelectric PbZrO₃ from atomistic simulations *Phys. Rev. B* **91** 134112
- [45] Íñiguez J, Stengel M, Prosandeev S and Bellaïche L 2014 First-principles study of the multimode antiferroelectric transition in PbZrO₃ *Phys. Rev. B* **90** 220103
- [46] Fthenakis Z G and Ponomareva I 2017 Dynamics of antiferroelectric phase transition in PbZrO₃ *Phys. Rev. B* **96** 184110
- [47] Gonze X et al 2016 Recent developments in the ABINIT software package *Comput. Phys. Commun.* **205** 106–31
- [48] Gonze X et al 2009 First-principles approach to material and nanosystem properties *Comput. Phys. Commun.* **180** 2582–615
- [49] Nakata A et al 2020 Large scale and linear scaling DFT with the CONQUEST code *J. Chem. Phys.* **152** 164112
- [50] Hamann D R 2013 Optimized norm-conserving Vanderbilt pseudopotentials *Phys. Rev. B* **88** 085117
- [51] van Setten M, Giantomassi M, Bousquet E, Verstraete M, Hamann D, Gonze X and Rignanese G-M 2018 The PseudoDojo: training and grading a 85 element optimized norm-conserving pseudopotential table *Comput. Phys. Commun.* **226** 39–54
- [52] Perdew J P, Ruzsinszky A, Csonka G I, Vydrov O A, Scuseria G E, Constantin L A, Zhou X and Burke K 2008 Restoring the density-gradient expansion for exchange in solids and surfaces *Phys. Rev. Lett.* **100** 136406

- [53] Marques M A, Oliveira M J and Burnus T 2012 Libxc: a library of exchange and correlation functionals for density functional theory *Comput. Phys. Commun.* **183** 2272–81
- [54] Zhang Y, Sun J, Perdew J P and Wu X 2017 Comparative first-principles studies of prototypical ferroelectric materials by LDA, GGA, and SCAN meta-GGA *Phys. Rev. B* **96** 035143
- [55] Monkhorst H J and Pack J D 1976 Special points for Brillouin-zone integrations *Phys. Rev. B* **13** 5188
- [56] Yu M and Trinkle D R 2011 Accurate and efficient algorithm for Bader charge integration *J. Chem. Phys.* **134** 064111
- [57] Tang W, Sanville E and Henkelman G 2009 A grid-based Bader analysis algorithm without lattice bias *J. Phys.: Condens. Matter.* **21** 084204
- [58] Sanville E, Kenny S D, Smith R and Henkelman G 2007 Improved grid-based algorithm for Bader charge allocation *J. Comput. Chem.* **28** 899–908
- [59] Henkelman G, Arnaldsson A and Jónsson H 2006 A fast and robust algorithm for Bader decomposition of charge density *Comput. Mater. Sci.* **36** 354–60
- [60] Campbell B J, Stokes H T, Tanner D E and Hatch D M 2006 ISODISPLACE: a web-based tool for exploring structural distortions *J. Appl. Crystallogr.* **39** 607–14
- [61] Artacho E, Snchez-Portal D, Ordejón P, García A and Soler J 1999 Linear-scaling *ab-initio* calculations for large and complex systems *Phys. Status Solidi b* **215** 809–17
- [62] Oroya J, Martín A, Callejo M, García-Mota M and Marchesin F 2020 Pseudopotential and numerical atomic orbitals basis dataset (Gipuzkoa: SIMUNE Atomistics)
- [63] Troullier N and Martins J L 1991 Efficient pseudopotentials for plane-wave calculations *Phys. Rev. B* **43** 1993
- [64] Zhong W, King-Smith R D and Vanderbilt D 1994 Giant LO–TO splittings in perovskite ferroelectrics *Phys. Rev. Lett.* **72** 3618
- [65] Goldschmidt V M 1926 The laws of crystal chemistry *Naturwissenschaften* **14** 477–85
- [66] Bartel C J, Sutton C, Goldsmith B R, Ouyang R, Musgrave C B, Ghiringhelli L M and Scheffler M 2019 New tolerance factor to predict the stability of perovskite oxides and halides *Sci. Adv.* **5** eaav0693
- [67] Anderson P 1960 *Izv. Akad. Nauk SSSR* 290
- [68] Resta R 1999 Macroscopic polarization from electronic wave functions *Int. J. Quantum Chem.* **75** 599–606
- [69] Resta R 1994 Macroscopic polarization in crystalline dielectrics: the geometric phase approach *Rev. Mod. Phys.* **66** 899–915
- [70] Berry M V 1984 Quantal phase factors accompanying adiabatic changes *Proc. R. Soc. A* **392** 45–57
- [71] King-Smith R D and Vanderbilt D 1993 Theory of polarization of crystalline solids *Phys. Rev. B* **47** 1651